nature geoscience

ARTICLES

https://doi.org/10.1038/s41561-022-00914-5

Check for updates

Crater population on asteroid (101955) Bennu indicates impact armouring and a young surface

E. B. Bierhaus[1]✉, D. Trang[2], R. T. Daly[3], C. A. Bennett[4], O. S. Barnouin[3], K. J. Walsh[5], R.-L. Ballouz[4], W. F. Bottke[5], K. N. Burke[4], M. E. Perry[3], E. R. Jawin[6,7], T. J. McCoy[6], H. C. Connolly Jr.[8,4], M. G. Daly[9], J. P. Dworkin[10], D. N. DellaGiustina[4], P. L. Gay[11], J. I. Brodbeck[4], J. Nolau[12], J. Padilla[4], S. Stewart[4], S. Schwartz[4,11], P. Michel[13], M. Pajola[14] and D. S. Lauretta[4]

The impactor-to-crater size scaling relationships that enable estimates of planetary surface ages rely on an accurate formulation of impactor–target physics. An armouring regime, specific to rubble-pile surfaces, has been proposed to occur when an impactor is comparable in diameter to a target surface particle (for example, a boulder). Armouring is proposed to reduce crater diameter, or prevent crater formation in the asteroid surface, at small crater diameters. Here, using measurements of 1,560 craters on the rubble-pile asteroid (101955) Bennu, we show that the boulder population controls a transition from crater formation to armouring at crater diameters ~2–3 m, below which crater formation in the bulk surface is increasingly rare. By combining estimates of impactor flux with the armouring scaling relationship, we find that Bennu's crater retention age (surface age derived from crater abundance) spans from 1.6–2.2 Myr for craters less than a few meters to ~10–65 Myr for craters >100 m in diameter, reducing the maximum surface age by a factor of >15 relative to previous estimates. The range of crater retention ages, together with latitudinal variations in large-crater spatial density, indicate that ongoing resurfacing processes render the surface many times younger than the bulk asteroid.

Impact cratering is ubiquitous across the Solar System[1] and is a major process driving surface evolution on asteroids[2–7]. Impact scaling relationships[8–10] relate properties of the impactor, target surface and resulting crater and are necessary to translate an observed crater population into a crater retention age (the age recorded by the craters themselves[11,12]). Crater retention ages are thus sensitive to the accuracy of such scaling relationships.

Historically, these scaling relationships were motivated by observations of planets and larger moons and generally have assumed crater formation to occur in either the strength or gravity regimes (see ref. [13] and Methods), depending on whether strength or surface gravity halts crater formation. However, for rubble-pile asteroids, which consist of unconsolidated blocks and regolith, their microgravity and potential low strength[14] make this demarcation ambiguous. Further, impacts into blocks surrounded by regolith lead to varying outcomes depending on how deeply the block resides within the surrounding regolith[15]. The Hayabusa mission to the rubble-pile asteroid Itokawa observed craters that contrast morphologically with those on larger asteroids and planetary surfaces[7], prompting investigations of impact cratering on rubble-pile surfaces[16–18].

Laboratory experiments[17] indicated two fundamental 'armouring' behaviours for impacts when the target particle size is comparable to the impactor size. The first type of armouring occurs when the impactor is smaller than the target particle but exceeds the disruption energy of the particle, resulting in a reduced crater size. The second armouring type prevents the formation of a crater in the bulk asteroid surface and occurs when the impactor is smaller than, and has less energy than the disruption threshold of, the target particle, although a crater may form on the target particle[19]. The proposed armouring scaling[17] transitions to gravity scaling above the armouring diameters. The Hayabusa2 Small Carry-on Impactor (SCI) experiment at the rubble-pile asteroid Ryugu, which entailed firing a projectile at the asteroid's surface, formed a ~15-m-diameter crater in the gravity regime, or in a very low-strength surface[20], consistent with the scaling prediction. Crater retention ages of Itokawa derived by taking these armouring behaviours into account are consistent with cosmic-ray exposure ages[17].

Our definition of 'armouring' follows the suggestion, first introduced in analysis of craters on Eros[2], that a spatially dense population of surface boulders limits and even prevents the formation of craters that would otherwise form in fine-grained regolith, that is, that the surface boulders 'armour' against impact crater formation. 'Armouring' is also used to describe effects stemming from particle-size sorting in terrestrial processes, for example, the concentration of larger particles by removing smaller particles by fluid action[21]. There are common characteristics between the two concepts (particle-size-dependent effects). However, our use here is specific to a surface boulder population's effect on impact cratering. We use 'boulder' inter-changeably with 'target particle' because the sizes of interest are generally >25 cm, above which particles are classified as boulders.

The global coverage and high spatial resolution data collected by the Origins, Spectral Interpretation, Resource Identification,

[1]Lockheed Martin Space, Littleton, CO, USA. [2]Hawai'i Institute of Geophysics and Planetology, University of Hawai'i at Mānoa, Honolulu, HI, USA. [3]Johns Hopkins University Applied Physics Laboratory, Laurel, MD, USA. [4]Lunar and Planetary Laboratory, University of Arizona, Tucson, AZ, USA. [5]Southwest Research Institute, Boulder, CO, USA. [6]Smithsonian Institution National Museum of Natural History, Washington, DC, USA. [7]Smithsonian Institution National Air and Space Museum, Washington, DC, USA. [8]Department of Geology, Rowan University, Glassboro, NJ, USA. [9]Centre for Research in Earth and Space Science, York University, Toronto, Canada. [10]Solar System Exploration Division, NASA Goddard Spaceflight Center, Greenbelt, MD, USA. [11]Planetary Science Institute, Tucson, AZ, USA. [12]Department of Physics, University of Central Florida, Orlando, FL, USA. [13]Observatoire de la Côte d'Azur, CNRS, Laboratoire Lagrange, Université Côte d'Azur, Nice, France. [14]INAF-Astronomical Observatory of Padova, Padova, Italy. ✉e-mail: edward.b.bierhaus@lmco.com

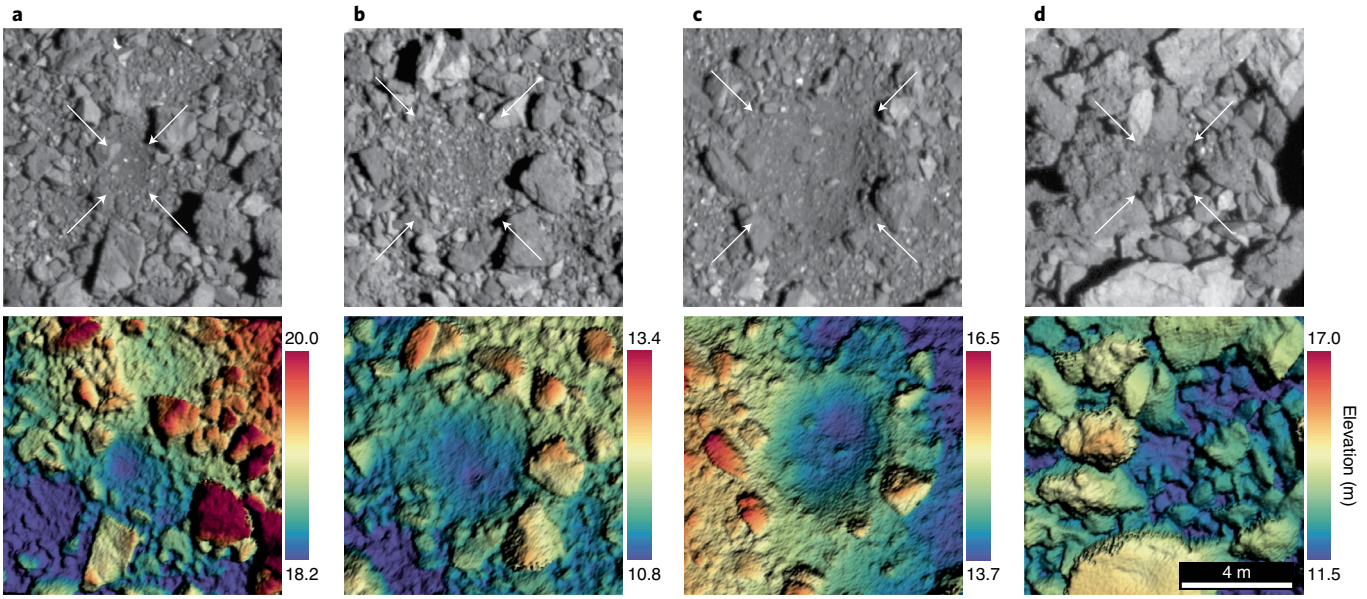

Fig. 1 | Examples of small craters on Bennu. a–d, Craters measuring 1.6 m (**a**), 4 m (**b**) and 6 m (**c**) in diameter, and 2.7 m in long axis for the irregularly shaped depression (**d**). Top: PolyCam[25] images. Bottom: DTMs constructed from OLA data[26–29]. White arrows indicate the boundaries of the craters. The scale bar in the bottom panel of **d** applies to all panels. Unlike larger craters on Bennu, or craters on larger planetary surfaces, these craters do not have distinct rims surrounding a depression. Rather, they often are enclosed, completely or partially, by a 'campfire ring' of boulders that were displaced by the impact. In addition, on average, particle sizes are smaller inside the craters than outside. PolyCam images are ocams20190321t194711s237_pol_iofl2_pan (**a**), ocams20190321t211320s080_pol_iofl2pan (**b**), ocams20190321t205607s955_pol_iofl2pan (**c**) and ocams20190321t181825s151_pol_iofl2pan (**d**).

and Security–Explorer (OSIRIS-REx) spacecraft at the rubble-pile asteroid Bennu[22] make it possible to test the impact-armouring paradigm. Data from the OSIRIS-REx mission have thus far been used to estimate surface age by analysing early observations of the crater population assuming a strength regime[23], evaluating pit craters formed on boulders[19] and evaluating colour variations within the small-crater population[24]. Here, we provide a complete, global database of the crater population on Bennu and evaluate the ability of the strength, gravity and armouring scaling regimes to explain the observed crater size–frequency distribution, and derived crater retention ages.

Size–frequency distribution of craters on Bennu

We identified and measured craters on Bennu using OSIRIS-REx Camera Suite (OCAMS[25]) images, and digital terrain models (DTMs[26–28]) generated from the OSIRIS-REx Laser Altimeter (OLA[29]) data. For both data types, we identified and measured craters using the Small Body Mapping Tool (SBMT[30]), which can simultaneously render images and DTMs, enabling an assessment of the asteroid surface in three dimensions. We also engaged citizen scientists for image-based crater identification (Methods).

Larger craters on Bennu (Extended Data Fig. 1) are identifiable by the presence of circular or elliptical features with raised rims and/or depressed floors. Smaller craters (less than ~10 m diameter) often lack raised rims. However, they can have a surrounding ring of boulders, and/or exhibit smaller particle sizes within crater interiors (Fig. 1), which often correspond to spectrophotometric changes in visible wavelengths[24].

Our global crater database consists of 1,560 craters with diameter from <1 m to over 200 m. The size–frequency distribution (SFD) is shown in Fig. 2. Below ~2.3 m diameter (the weighted mid-point of a diameter bin that spans 2–3 m), the number density of craters decreases rapidly. Because of the appearance of the small-crater SFD in differential format (Fig. 2c), we refer to this shape as a 'fishhook'. The decrease is not simply a subtle change in power-law slope. Rather, the population density peaks at the diameter bin centred at 2.3 m and trends rapidly towards zero. The abundance of ~1 m craters is smaller by more than ten fold compared with what would be predicted by the trend from larger craters. Before exploring physical reasons for this fall-off, we first must rule out the possibility that it is an artefact of observational limitations.

Previous analysis[31] suggested a typical ~10 pixel completeness limit, below which features may be identified but catalogues are incomplete owing to the finite resolution of the image data. The decrease in crater density for diameters <3 m in Fig. 2c corresponds to 46 PolyCam pixels and 23 DTM post-spacings (Extended Data Table 1). This is four and two times greater, respectively, than the 10 pixel completeness limit. The PolyCam images have a point-spread function <2 pixels and were not compressed. The lighting and viewing geometries of these images have moderate incidence angles for shadowing and low emission angles, the preferred combination for identification and morphological analysis. The polar regions were observed by both cameras and lidar during orbital phases, enabling crater measurements at all latitudes, although the best images of the polar regions, and the OLA DTMs, are lower in spatial resolution than the best available images of regions within ±60° latitude. The lower spatial resolution of the OLA DTMs could lead to fewer small-crater detections in the poles. To avoid potential bias in these regions, we filtered the craters to include all diameters within ±60° and only diameters >5 m poleward of 60° (Extended Data Fig. 2a). The resulting population preserves the fishhook shape. Thus, we eliminate finite spatial resolution of the data as the cause for the decrease in crater density below ~3 m diameter.

With this confirmation that the population decrease of small craters is not an observational artefact, we consider physical processes that could erase small craters: seismic shaking and mass wasting.

Seismic shaking by impact has been invoked[32] to explain erosion of craters on asteroids. Modelled effects assume erasure efficiencies sufficient for more frequently formed smaller craters to erase larger craters, leading to fewer observable craters. However, the resultant crater population still has an increasing number of smaller craters. To explain the rapid loss of ~2 m craters via seismic shaking would

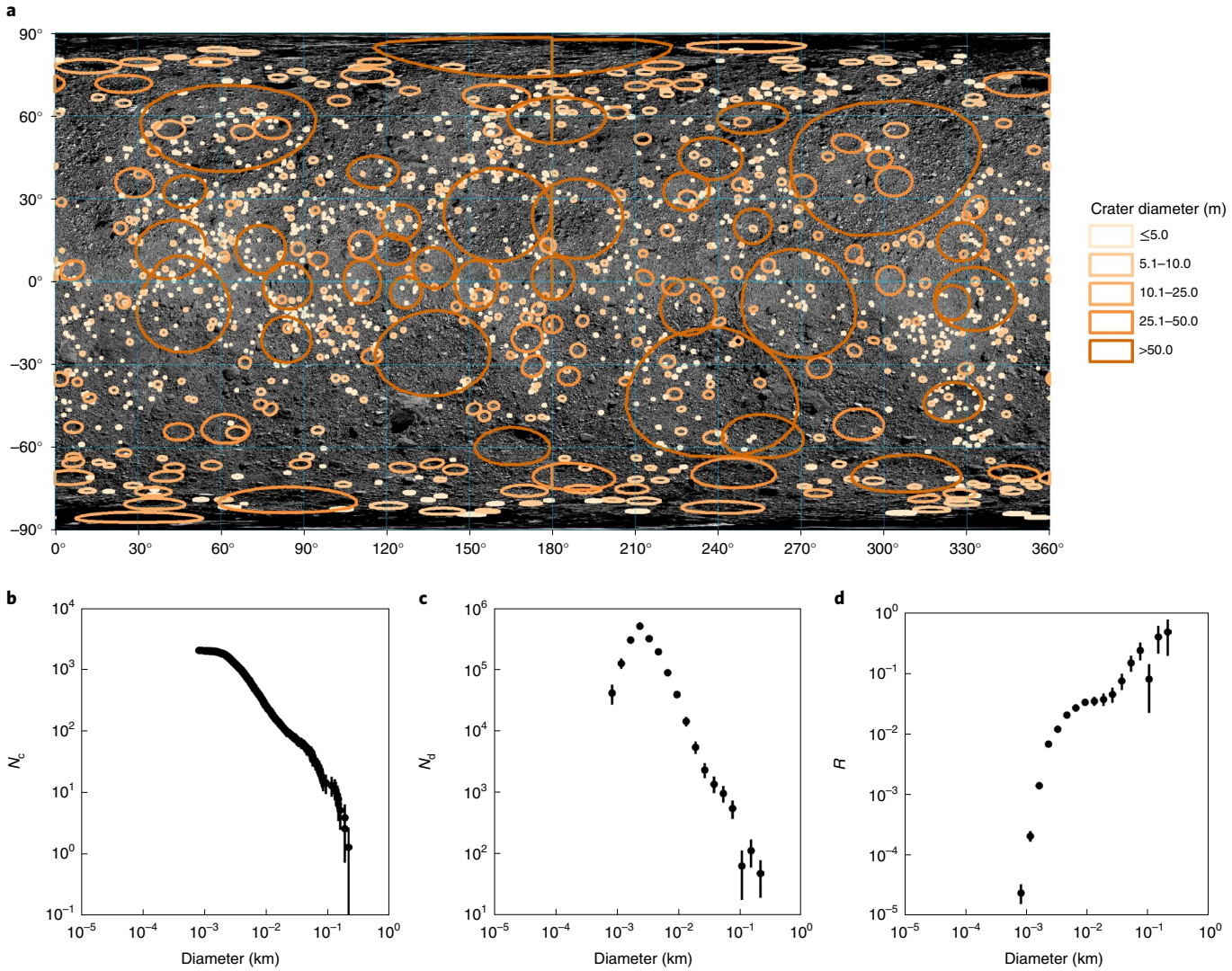

Fig. 2 | Bennu's crater population. a, Global distribution of Bennu's craters in a simple cylindrical projection, layered over an image basemap[55]. **b**–**d**, The cumulative (**b**), differential (**c**) and relative SFD (**d**) of the crater population. In all plots, the error bars are $\sqrt{N}$ for Poisson counting statistics. The area used for normalization is 0.787 km^2 (the global surface area of Bennu[28]). Each form of the SFD highlights different aspects of the population. The cumulative distribution shown in **b** is $N_c = N(D > D')/A$, where $N(D > D')$ is the number of craters with diameter $D > D'$, and A is the surface area of Bennu, which is often used for age estimates. We provide it here as a reference to compare with the other datasets. The differential distribution shown in **c** is $N_d = dN/(dD\ A)$, where dN is the number of craters with diameter in the range dD, which is a more direct representation of the number of craters present at any given size. The plot here highlights a transition from an increasing number of smaller craters, as diameters decrease, until the diameter bin centred at 2.3 m (spanning 2–3 m), at which point the population of craters instead decreases at smaller diameters, giving the distribution a shape resembling a fishhook. The relative plot shown in **d** is $R = N_d/D^{-3}$, which is the differential data normalized by a differential exponent of −3 (that is, a differential population with an exponent of −3 would plot as a horizontal line), demonstrating that the population does not follow a single power-law exponent over the measured diameters.

require there to be more 1 m craters than 2 m craters, yet we observe fewer craters at progressively smaller sizes on Bennu. Also, observations[33,34] from the region immediately around the Hayabusa2 SCI crater on Ryugu indicate low translation of impact energy into seismic shaking, limiting the effect to an area within a few crater radii of the impact site.

Localized regions of recent mass movement have been observed on Bennu that appear correlated with recent changes in spin rate and slope instabilities[35]. There are strong global trends for higher slope at higher latitude[36], yet the fishhook shape is identical when the equator is analysed separately from the northern or southern mid-latitudes (Extended Data Fig. 2b). If these mass movements erased small craters, the small-crater abundance would be anti-correlated with slope. However, we find the spatial density of craters 1–3 m in diameter (that is, in the fishhook transition from increasing to decreasing number density) are not correlated with regions of high slope (Fig. 3). Crater depth-to-diameter ratios are not correlated with slope either[37], contrary to expectations if mass wasting caused in-filling of small craters. Thus, although mass movement may erase some small craters immediately adjacent to high-slope regions, it cannot account for the global under-abundance of craters less than 3 m in diameter.

Because of the inconsistency between the observed crater SFD (decreased abundance of small craters) and what would be expected for seismic shaking (which preserves an increasing number of small craters), and the non-correlation between slope and small craters,

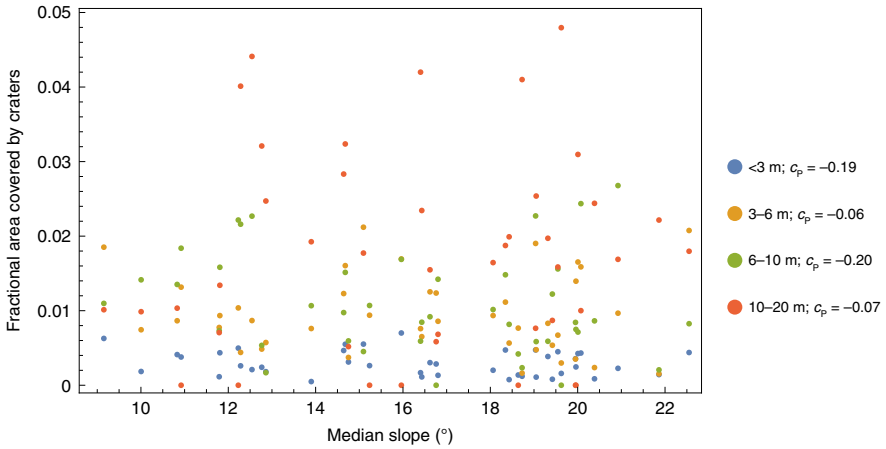

Fig. 3 | Fractional area covered by craters versus surface slope for craters ≤20 m diameter, binned into different diameter ranges. The plot legend identifies the colours for the different crater-diameter bins, as well as the Pearson coefficient for the fractional area versus slope of that diameter range. The Pearson coefficient (c_p) evaluates whether two parameters are correlated: $c_p = -1$ indicates perfect anti-correlation, $c_p = +1$ indicates perfect correlation and $c_p = 0$ indicates no correlation. The absolute magnitude of the Pearson coefficient never exceeds 0.2. The low correlation between slope and fractional area covered by craters indicates that mass-wasting processes cannot explain the significant under-abundance of craters <3 m.

we eliminate crater-erasure mechanisms as the cause for the rapid decrease in crater density below 3 m.

Secondary craters[38] (impact craters formed by the impact of material ejected during a primary impact) should not be present on Bennu because of the low escape speed. Secondary craters form because an object's surface gravity is sufficient to retain ejecta moving fast enough to form a crater. Observations of ejected boulders around lunar craters[39,40] and secondary craters on mid-sized icy satellites[41] suggest that the minimum speed for a secondary crater is on the order of 100 m s^{-1}. In contrast, material can escape[42,43] Bennu at speeds as low as 10 cm s^{-1} and always escapes Bennu at speeds greater than ~30 cm s^{-1}. These speeds are three orders of magnitude smaller, with impact energies ~10^6 smaller, than those associated with the minimum needed to form secondary craters. We thus conclude that secondaries do not form on Bennu and, unlike for larger bodies[44], do not need to be a consideration for derived surface ages.

Fitting the distribution and deriving ages with armouring

Notable features of the crater SFD include (1) the fishhook structure described above, (2) a decrease in large-crater density around 100 m diameter and (3) the fact that the overall crater SFD does not follow a single power law (Fig. 2d). We examine each of these features in turn.

Evaluation of small-crater SFD. We hypothesize that the fishhook shape of the crater SFD at small diameters in Fig. 2b reveals a transition from cratering in the bulk surface to armouring. To evaluate this hypothesis, we developed a model that accounts for armouring derived from a rubble-pile impact scaling relationship[17] (hereafter, TS2018 scaling; Methods and Extended Data Table 2) to compare with observations. Unlike gravity or strength scaling, a possible outcome for an impactor using TS2018 scaling is a failure to make a crater in the bulk asteroid surface. Whether a crater forms, and the diameter of the resulting crater if created, depends on the sizes of both the impactor and the target boulder. Thus, to model crater production, we generated both impactor and target particle sizes in a Monte Carlo fashion (Methods). To determine impactor sizes, we used estimates of the impactor flux both in the main belt and in near-Earth space, because Bennu formed as a main-belt asteroid (MBA) and evolved to be a near-Earth asteroid[45] (NEA). To determine boulder sizes, we used the observed boulder SFD[46,47]. Because modelling the crater population for a given surface age is probabilistic with this technique, we generate 100 cases for each age to develop statistics on the potential range of outcomes (Extended Data Fig. 3a). Implementation of the TS2018 scaling reproduces the fishhook shape of the small-crater SFD (Fig. 4a). This unusual SFD results from a transition from impactor energies sufficiently high to form a crater to energies insufficient to disrupt a target surface boulder. The fishhook shape is a robust outcome as long as this transition in crater formation occurs.

The crater-diameter range of this fishhook feature is a function of the boulder population SFD, whose presence begins to frustrate crater formation. In addition, the vertical location of the crater SFD peak provides a unique constraint on the crater retention age by matching the fishhook location of the differential crater SFD (Fig. 4a). Because we evaluate the model's ability to recreate the fishhook, our comparison between the data and model uses the binned, differential version of the data. We evaluate multiple diameter-bin combinations when deriving surface ages (Extended Data Fig. 3b,c). The minimum residuals between the small-crater observations and models occur for an age range between 1.6 and 2.2 Myr (Extended Data Fig. 4a–f), using an NEA impactor flux[48,49].

Evaluation of the largest-crater SFD. The TS2018 scaling relationship approximates the gravity-scaling regime at larger diameters[17]. Spacecraft observations support the transition from armouring to gravity scaling as diameters increase. The SCI experiment performed by the Hayabusa2 mission at Ryugu indicates a maximum cratering strength on that rubble-pile asteroid of <1.3 Pa (ref. [20]). Similarly, the discovery of impact-ejecta effects adjacent to a crater rim, despite Bennu's microgravity environment, implies a maximum cratering strength[50] consistent with the SCI. Thus, we apply TS2018 scaling to model the largest craters. Although Bennu's surface gravity varies by approximately two fold from equator to pole[51], the difference in gravity-scaled diameter is negligible for crater diameters observed on Bennu (Extended Data Fig. 5).

Large-crater abundance establishes the maximum crater retention age (because large impactors are the least frequent), thus we consider model fits to combinations of the five largest-diameter bins. Based on 99% minimum residuals and an NEA flux, we find a >100 Myr retention age to create the largest craters (Extended Data Fig. 4g–k). This age is unreasonably large compared with Bennu's expected NEA lifetime of ~1.75 Myr (ref. [19]) or 2.6 Myr (ref. [48]) and

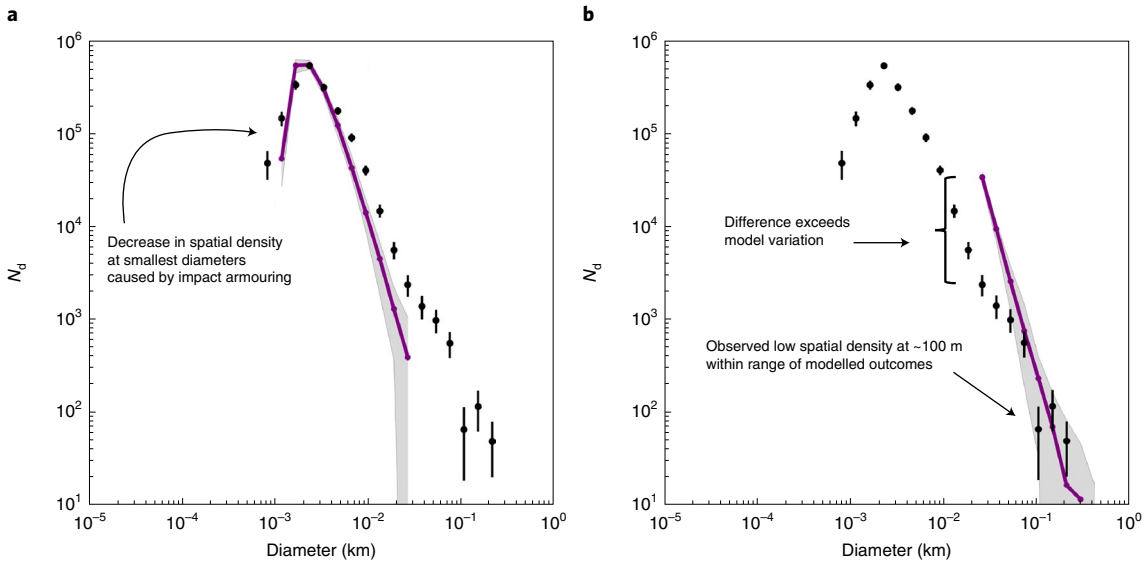

Fig. 4 | Observed crater differential SFD compared with model results. a, The 2.0 Myr results for the modelled NEA flux. The black points are the same data as in Fig. 2. The purple data are the median results from 100 runs of a 2 Myr age, and the grey-shaded band represents the range of 99% of the simulations. Unlike traditional strength or gravity results, the TS2018 model crater population reaches a maximum value (at a crater diameter location controlled by the boulder population), then decreases owing to the armouring effect that occurs when the projectile size and energy are comparable to the sizes and disruption energies of boulders on the surface. **b**, The 30 Myr results for the modelled MBA flux (colours as in **a**). The difference between modelled and observed craters tens of metres in size is greater than the variation in the modelled outcomes. In contrast, the observed low density of craters with ~100 m diameter is within the modelled outcomes. Because the number of impactors at small diameters exceeds 10^9 for this age, the model impact flux was truncated to diameters that create the largest craters. See Methods for details on the model description and the residuals for the model fits.

the 10 Myr mean lifetime of NEAs[52]. Thus, the largest craters must have formed when Bennu's orbit maintained collisional interaction with the main belt. Using the MBA flux, we derive a crater retention age of 10–65 Myr for the largest craters (Extended Data Fig. 6). Although the diameter bin at ~100 m has a low abundance compared with adjacent bins, the magnitude of this decrease is within the span of modelled outcomes for every age evaluated between 10 to 65 Myr (Extended Data Fig. 6f,g).

Size-dependent variability. The crater production that best fits the largest craters overpredicts the number of craters with diameters less than ~40 m. Figure 4a,b suggests that the majority of Bennu's crater population reflects two epochs: the large craters that accumulated while Bennu was still in collisional communication with the main belt, and the small craters from Bennu's residence as an NEA. We summarize our assessment of Bennu's crater SFD as follows (see annotations in Fig. 4a,b): (i) the observed decrease in density below 3 m is caused by impact armouring, (ii) the under-abundance (relative to the largest craters) of craters tens of meters in diameter exceeds the range of modelled outcomes and thus reflects erasure at these sizes since the formation of the largest and oldest craters and (iii) the observed ~100-m-diameter bin, which is within the range of the modelled outcomes.

Small-crater abundances are not correlated with slope (Fig. 3) and nor is the appearance of the fishhook shape in the differential SFD (Extended Data Fig. 2b). In contrast, the abundance of larger craters, which form infrequently compared with the diameters that define the fishhook shape, are correlated with slope and latitude (Extended Data Fig. 7). This distinction in slope dependence between large and small craters suggests that mass wasting[35] due to slope failure removed some larger craters prior to Bennu's residence as an NEA. Craters then formed on the new surfaces, with impact armouring suppressing crater formation at diameters less than ~3 m.

Armouring implications for surface processes and age

A small fraction of impactors make craters in Bennu's bulk surface using TS2018 scaling. For example, only 4% of our modelled NEA flux (we modelled impactors between 5.7×10^{-3} and 0.35 m) made impact craters. The remainder hit a boulder large enough to prevent the formation of a crater in the bulk surface. This suggests that crater formation in boulders[19], and boulder disruption, are more common than crater formation, and that the collisional displacement and disruption of surface boulders by small impactors is a major and rapid process in rubble-pile surface evolution. This scenario may apply to all rubble-pile objects.

A small-crater retention age of ~2 Myr is among the youngest observed in the Solar System. This young crater retention age indicates that geologically rapid processes can occur even on small worlds that lack internally driven surface changes. Earlier estimates of surface ages, using the same NEA flux as our analysis[44], concluded that Bennu has been an NEA for ~1.75 Myr (ref. [19]) and a crater retention age of $<10^5$ yrs for a subset of the small craters (<10 m) with the reddest colours[24]. These works agree with our assessment that the majority of Bennu's smallest craters (diameters <5 m; Extended Data Fig. 8a) formed during its time as an NEA.

A previous analysis of Bennu[23] reported a large-crater retention age of 100 Myr to 1 Gyr. The discrepancy with our results is because that study assumed a strength-scaling regime with 0.18 MPa cratering strength, whereas the ages we derive are based on TS2018 scaling. Some strength in Bennu's subsurface may affect the formation of the very largest craters, as evidenced by the decrease in crater depth-to-diameter ratios at larger diameters[37] and the existence of longitudinal ridges and other topographic features implying some internal stiffness[28,52]. If the cratering strength is ≤100 Pa, as inferred from observations of a 70-m-diameter crater with an ejecta field[50], strength-scaling results for large craters are comparable to those from TS2018 scaling (Extended Data Fig. 8a).

The spatial density of Bennu's largest craters is like that of Itokawa's, and both Bennu and Itokawa have higher crater spatial density than Ryugu for diameters >100 m (Extended Data Fig. 8b–d). Previous analyses using the TS2018 scaling approach found that Itokawa's crater retention age is 3–33 Myr (ref. [17]) and Ryugu's crater retention age is 8.9 ± 2.5 Myr (ref. [20]). Our derived range of 10–65 Myr for Bennu's largest craters overlaps with the age ranges of the other two asteroids. The Itokawa data appear to have a peak diameter in differential format at ~16 m, and a broader fishhook shape, which may be due to differences in composition that lead to higher disruption strength for surface boulders on Itokawa. Ryugu's crater SFD does not exhibit a fishhook, although that may be due to the minimum-sized crater in the dataset, which is 10 m. Ryugu does show a change in the SFD slope at ~40 m, which may represent a transition to smaller crater diameters caused by armouring.

The maximum crater retention age from our analysis (65 Myr) is younger by over an order of magnitude than the predicted age of Bennu as a distinct planetary object (~1 Gyr (ref. [48])), suggesting that it has been resurfaced since it formed. This is also consistent with the possibility that Bennu is an '*n*th generation rubble pile'. That is, it has been partly or fully disrupted more than one time since it originally formed from the reaccumulating fragments of a parent-body disruption[53,54].

Online content

Any methods, additional references, Nature Research reporting summaries, source data, extended data, supplementary information, acknowledgements, peer review information; details of author contributions and competing interests; and statements of data and code availability are available at https://doi.org/10.1038/s41561-022-00914-5.

Received: 15 April 2021; Accepted: 18 February 2022;
Published online: 07 April 2022

References

1. Melosh, H.J. *Impact Cratering, A Geologic Process* (Oxford University Press, 1989).
2. Chapman, C. R. et al. Impact history of Eros: craters and boulders. *Icarus* **155**, 104–118 (2002).
3. Chapman, C. R., Veverka, J., Belton, M. J. S., Neukum, G. & Morrison, D. Cratering on Gaspra. *Icarus* **120**, 77–86 (1996a).
4. Chapman, C. R. et al. Cratering on Ida. *Icarus* **120**, 231–245 (1996b).
5. Geissler, P. et al. Erosion and ejecta reaccretion on 243 Ida and its moon. *Icarus* **120**, 140–157 (1996).
6. Hirata, N. et al. The spatial distribution of impact craters on Ryugu. *Icarus* https://doi.org/10.1016/j.icarus.2019.113527 (2020).
7. Hirata, N. et al. A survey of possible impact structures on 25143 Itokawa. *Icarus* **200**, 486–502 (2009).
8. Chabai, A. J. *Influence of Gravitational Fields and Atmospheric Pressures on Scaling of Explosion Craters. Impact and Explosion Cratering* (Pergamon, 1977).
9. Holsapple, K. A. The scaling of impact processes in planetary sciences. *Annu. Rev. Earth Planet Sci.*, **21**, 333–373 (1993).
10. Housen, K. R., Sweet, W. J. & Holsapple, K. A. Impacts into porous asteroids. *Icarus* **300**, 72–96 (2018).
11. Shoemaker E. M. in *The Nature of the Lunar Surface* (eds Heiss W. N., Menzel D. R. and O'Keefe J. A.) pp. 23–77 (Johns Hopkins Univ. Press, 1965).
12. Hartmann, W. K. & Neukum, G. Cratering chronology and the evolution of Mars. *Space Sci. Rev.* **96**, 165–194 (2001).
13. Holsapple, K. A. & Schmidt, R. M. On the scaling of crater dimensions. II – Impact processes. *J. Geophys. Res.* **v. 87**, 1849–1870 (1982).
14. Scheeres, D. J., Hartzell, C. M., Sanchez, P. & Swift, M. Scaling forces to asteroid surfaces: the role of cohesion. *Icarus* **210**, 968–984 (2010).
15. Durda, D. D. et al. Experimental investigation of the impact fragmentation of blocks embedded in regolith. *Meteorit. Planet. Sci.* **46**, 149–155 (2011).
16. Güttler, C., Hirata, N. & Nakamura, A. M. Cratering experiments on the self armoring of coarse-grained granular targets. *Icarus* **220**, 1040–1049 (2012).
17. Tatsumi, E. & Sugita, S. Cratering efficiency on coarse-grained targets: implications for the dynamical evolution of asteroid 25143 Itokawa. *Icarus* **300**, 227–248 (2018).
18. Barnouin, O. S., Daly, T. R., Cintala, M. J. & Crawford, D. A. Impacts into coarse-grained spheres at moderate impact velocities: implications for cratering on asteroids and planets. *Icarus* **325**, 67–83 (2019).
19. Ballouz, R. L. et al. Bennu's near-Earth lifetime of 1.75 million years inferred from craters on its boulders. *Nature* **587**, 205–209 (2020).
20. Arakawa, M. et al. An artificial impact on the asteroid (162173) Ryugu formed a crater in the gravity-dominated regime. *Science* **368**, 67–71 (2020).
21. Sutherland, A. J. in *Sediment Transport in Gravel Bed Rivers* (eds Thorne, C. R., Bathurst, J. C. and Hey, R. D.) pp 243–260 (Wiley, 1987).
22. Lauretta, D. S., Enos, H. L., Polit, A. T., Roper, H. L., Wolner, C. W. V. in *Sample Return Missions* (ed. Longobardo, A) ch. 8 (Elsevier, 2021).
23. Walsh, K. J. et al. Craters, boulders and regolith of (101955) Bennu indicative of an old and dynamic surface. *Nat. Geosci.* **12**, 242–246 (2019).
24. DellaGiustina, D. N. et al. Variations in color and reflectance on the surface of asteroid (101955) Bennu. *Science* 370, eabc3660 (2020).
25. Rizk, B. et al. OCAMS: the OSIRIS-REx camera suite. *Space Sci. Rev.* 214, 26 (2018).
26. Seabrook, J. A. et al Global shape modeling using the OSIRIS-REx scanning laser altimeter. *Planet. Space. Sci.* **177**, 104688 (2019).
27. Barnouin, O. S. et al. Digital terrain mapping by the OSIRIS-REx mission. *Planet. Space Sci.* **180**, 104764 (2020).
28. Daly, M. G. et al. Hemispherical differences in the shape and topography of asteroid (101955) Bennu. *Sci. Adv.* **6**, eabd3649 (2020).
29. Daly, M. G. et al. The OSIRIS-REx Laser Altimeter (OLA) investigation and instrument. *Space Sci. Rev.* **212**, 899–924 (2017).
30. Ernst, C.M., Barnouin, O.S., Daly, R.T. and the Small Body Mapping Tool Team. The Small Body Mapping Tool (SBMT) for accessing, visualizing, and analyzing spacecraft data in three dimensions. *The Lunar and Planetary Science Conference*, contribution no. 2083, id. 1043 (Lunar and Planetary Institute (LPI), 2018).
31. Robbins, S. J. et al. The variability of crater identification among expert and community crater analysts. *Icarus* **234**, 109–131 (2014).
32. Richardson, J.E., Steckloff, J.K. and Minton, D.A. Impact-produced seismic shaking and regolith growth on asteroids 433 Eros, 2867 Steins, and 25143 Itokawa. *Icarus* **347** https://doi.org/10.1016/j.icarus.2020.113811 (2020).
33. Nishiyama G. et al. Simulation of seismic wave propagation on asteroid Ryugu induced by the impact experiment of the Hayabusa2 mission: limited mass transport by low yield strength of porous regolith. *J. Geophys. Res. Planets* **126**, e06594 (2021).
34. Honda, R. et al. Resurfacing processes on asteroid (162173) Ryugu caused by an artificial impact of Hayabusa2's Small Carry-on Impactor. *Icarus* **366**, 114530 (2021).
35. Jawin E. R. et al. Global patterns of recent mass movement on asteroid (1011955) Bennu. *J. Geophys. Res. Planets*, **125**, E06475 (2020).
36. Scheeres, D. J., 40 colleagues. The dynamic geophysical environment of (101955) Bennu based on OSIRIS-REx measurements. *Nat. Astron.* **3**, 352–361 (2019).
37. Daly, T. et al. The morphometry of impact craters on Bennu. *Geophys. Res. Lett.* https://doi.org/10.1029/2020GL089672 (2020).
38. McEwen, A. S. & Bierhaus, E. B. The importance of secondary cratering to age constraints on planetary surfaces. *Annu. Rev. Earth Planet. Sci.* **34**, 540–567 (2006).
39. Bart G. D. and Melosh H. J. Impact into lunar regolith inhibits high-velocity ejection of large blocks. *J. Geophys. Res. Planets* **115**, E08004 (2010).
40. Bart, G. D. & Melosh, H. J. Distributions of boulders ejected from lunar craters. *Icarus* **209**, 337–357 (2010).
41. Bierhaus, E. B., Dones, L., Alvarellos, J. L. & Zahnle, K. The role of ejecta in the small crater populations on the mid-sized Saturnian satellites. *Icarus* **218**, 602–621 (2012).
42. McMahon, J.W. et al. Dynamical evolution of simulated particles ejected from asteroid Bennu. *J. Geophys. Res. Planets* **125**, e06229 (2020).
43. Bierhaus, E.B. et al. Bennu regolith mobilized by TAGSAM: expectations for the OSIRIS-REx sample collection event and application to understanding naturally ejected particles. *Icarus* **355**, 114142 (2021).
44. Bierhaus, E. B. et al. Secondary craters and ejecta across the solar system: populations and effects on impact-crater-based chronologies. *Meteorit. Planet. Sci.* **53**, 638–671 (2018).
45. Bottke, W. F. et al. Interpreting the cratering histories of Bennu, Ryugu, and other spacecraft-explored asteroids. *Astron. J.* **160**, 14 (2020).
46. DellaGiustina, D. N. et al. Properties of rubble-pile asteroid (101955) Bennu from OSIRIS-REx imaging and thermal analysis. *Nat. Astron.* **3**, 341–351 (2019).
47. Burke et al. Particle size-frequency distributions of the OSIRIS-REx candidate sample sites on asteroid (101955) Bennu. *Remote Sens.* **13**, 1315 (2021).
48. Bottke, W. F. et al. In search of the source of asteroid (101955) Bennu: applications of the stochastic YORP model. *Icarus* **247**, 191–217 (2015).

49. Brown, P., Spalding, R. E., ReVelle, D. O., Tagliaferri, E. & Worden, S. P. The flux of small near-Earth objects colliding with the Earth. *Nature* **420**, 294–296 (2002).
50. Perry, M. E. et al. Low surface strength of the asteroid Bennu inferred from impact ejecta deposit. *Nat. Geosci.* https://doi.org/10.1038/s41561-022-00937-y (2022).
51. Barnouin, O. S., OSIRIS-REx Team et al. Shape of (101955) Bennu indicative of a rubble pile with internal stiffness. *Nat. Geosci.* **12**, 247–252 (2019).
52. Gladman, B., Michel, P. & Froeschlé, C. The near-Earth object population. *Icarus* **146**, 176–189 (2000).
53. Walsh, K. J. et al. Likelihood for rubble-pile near-Earth asteroids to be 1st or *N*th generation: focus on Bennu and Ryugu. *LPSC*, LPI contribution no. 2326, id. 2253 (Lunar and Planetary Institute (LPI), 2020).
54. Michel, P. et al. Collisional formation of top-shaped asteroids and implications for the origins of Ryugu and Bennu. *Nat. Commun.* **11**, 2665 (2020).
55. Bennett, C. A. et al. A high-resolution global basemap of (101955) Bennu. *Icarus* https://doi.org/10.1016/j.icarus.2020.113690 (2020).

Publisher's note Springer Nature remains neutral with regard to jurisdictional claims in published maps and institutional affiliations.

© The Author(s), under exclusive licence to Springer Nature Limited 2022

Methods

Measurements of the crater population. This study used image data and lidar-derived DTMs (Extended Data Table 1) and relied on two groups of mappers to identify and measure the diameters of craters on Bennu: (1) experienced impact crater researchers and (2) citizen scientists. The experienced research group (the authors) used both images and the lidar-derived DTMs, whereas the citizen-science group only used images. Because of either high emission angles or shadowing in the polar regions, the DTMs were critical to identify and measure craters in those high-latitude regions.

Experienced researcher observations. We used calibrated images collected by the PolyCam and MapCam imagers of OCAMS[25,56] to identify craters on Bennu. For the largest craters, we used PolyCam images from the spacecraft's final approach so that a single image contains the measured crater (Extended Data Fig. 1). We used PolyCam images from Baseball Diamond Flybys 3 and 4 of the Detailed Survey phase to survey craters in the equatorial regions (0–40° latitude) because these flybys[57] provided emission angles <20°, which is an optimal angle to find impact craters. We used Orbital A images to survey the high-latitude and polar regions as images from this mission phase offered the lowest emission angle for these regions. However, all images of the polar regions exhibit high incidence angles, which results in significant shadowing that hampers crater identification. We projected all images onto the SPC (stereophotoclinometry) v22 global shape model[28] of Bennu using the SBMT[30], which assisted in accurately determining the location of each crater and its diameter. The SBMT provides tools to identify and measure features (called 'structures') in three dimensions. For the observed craters, we used a combination of circle and ellipse structures, and for both structure types, the SBMT records the centre location (latitude, longitude and radius) and size (diameter in the case of a circle; long axis and axial ratio in the case of an ellipse).

Citizen-scientist observations. Citizen scientists identified and measured craters through an application called Bennu Mappers, a program based on the Citizen Science Builder software package[58] and in collaboration with CosmoQuest. Previous versions of this application were successfully used to survey the Moon[31] and Vesta[59].

Citizen scientists identified craters using PolyCam images from the Flyby 3, 4A and 4B campaigns[55]. Images acquired during these campaigns highlighted surface features and minimized foreshortening and perspective distortion as Bennu was observed at low emission angles with incidence angles averaging between 30° and 50°. Between the three flybys, we achieved nearly global coverage[57] (±70° latitude). The images were radiometrically calibrated and displayed in units of reflectance[56] (that is, I/F, which is the ratio of scattered radiance, I, to the incident radiance, F), but unlike the images used by the experienced researchers, these images were not map-projected or shown on a shape model. Each 1,024×1,024 pixel image was split into 450×450 pixel subimages, which resulted in 4,500 individual subimages. Each subimage included a 22–50% overlap with neighbouring subimages. Due to the small coverage of each image, only craters <20 m could be identified.

Before making measurements, citizen scientists completed interactive training which included identifying and measuring the diameters of large and small boulders and craters on a simulated image of Bennu's surface. After training, citizen scientists worked sequentially on individual 450×450 pixel images. Afterwards, we combined the measurements of any craters that were identified by multiple citizen scientists by using a modified density-based spatial clustering of applications with noise algorithm[31] to convert these craters into a single data point (diameter and location). Our modifications to this algorithm included scaling the reachability parameter and the maximum clustering distance between craters. Finally, the experienced researchers evaluated each crater identified by citizen scientists.

OLA-based observations. Because OLA is insensitive to lighting conditions, the lidar-derived DTMs are ideal for surveying high-latitude regions for craters. We evaluated 10 cm post-spacing DTMs that are based on OLA data from the Orbital B phase[29]. We searched for craters in the DTMs using two different techniques. In the first technique, we visually identified craters by applying a greyscale value to the elevations and changing the difference between the minimum and maximum vertical greyscale values. As a result, larger differences allowed identification of deeper craters, whereas smaller differences allowed identification of shallower craters. In our second technique, we derived several shaded relief maps from the DTMs by systematically changing the azimuth angle of the artificial light source. This allowed us to identify craters through the use of shadows.

Global dataset. The combined measurements generated a global database of 1,560 craters from <1 m to over 200 m. A polar orbit permitted imaging and lidar data collection of the polar regions (Extended Data Table 1), but the best imaging and the lidar post-spacing is lower resolution than the image data available for ±60° latitude. To avoid potential detection biases for the smallest craters, we make a global SFD that includes all craters observed within ±60° latitude, and craters >5 m for higher latitudes (Extended Data Fig. 2a). We measured crater sizes by marking rim-crest diameters, bounding ring of boulder diameter, or particle-size contrast, depending on the crater morphology. The median variation in the measured diameter[37], including craters on slopes, is 12%. The SFD analysis presented here uses bin sizes of $\sqrt{2}\,D$ (~1.4D), wider than the median uncertainty in measured diameter.

Extended Data Fig. 2b shows that the fishhook shape appears in the crater sub-populations in distinct latitude/slope regions[35,36] on Bennu. In contrast, Extended Data Fig. 7 shows there is an anti-correlation between large-crater abundance and surface slope. That is, higher slope corresponds to lower fractional coverage by large craters. Because larger craters are generally older and smallest craters are the youngest impacts on Bennu, the relationships between crater size, abundance, latitude and slope indicate scale- and rate-dependent effects. The loss of larger craters in higher-slope/mid-latitude regions points to larger-scale, slope-related erasure processes occurring in Bennu's more distant past. Since that time, small craters have accumulated, leading to a super-position of small, recent craters over the remaining larger, older craters. This explains the ~two-epoch appearance of the SFD in Fig. 4.

Crater scaling relationships: strength, gravity and TS2018. The scaling relationship used to convert impactor size to crater size has a substantive effect on derived surface ages. If a smaller, more frequent impactor can make a given-sized crater, then the surface age is younger than would be predicted if one were to assume that a larger, less frequent impactor is needed to make that crater. Below we summarize widely used crater π-scaling relationships in the established strength and gravity regimes, as well as armouring scaling relationships[17] (TS2018) that add dimensionless terms to describe cratering in the armouring regime, then apply those results to craters on Bennu. Extended Data Table 2 lists the variables and values used for this analysis.

Strength regime. The strength metric Y used in crater scaling relationships is not one of the classic strength metrics, such as compressive, shear or tensile strength. That is because all three mechanical pressures occur during an impact. Thus, strength in this context is referred to as 'cratering strength'. Other research[60] has discussed the subtleties associated with interpreting what strength means for a cratering event, suggesting that, when comparing cratering events between like materials, shear strength may be the most appropriate strength metric, although even that can be complicated by a 'crushing strength' introduced by porosity. The strength regime formulation is[60]

$$R = \left(\frac{\rho}{m_\mathrm{p}}\right)^{-1/3} H_2 \left(\frac{\rho}{\delta}\right)^{\frac{1-3\nu}{3}} \left(\frac{Y}{\rho U^2}\right)^{-\mu/2}. \quad (1)$$

To compare with other formulations used for Bennu's craters[23], we recast in terms of impactor diameter, where $m_\mathrm{p} = \delta 4\pi a^3/3$. Substituting into equation (1), this gives

$$\frac{R}{a} = \left(\frac{3}{4\pi}\right)^{-1/3} H_2 \left(\frac{\rho}{\delta}\right)^{-\nu} \left(\frac{Y}{\rho U^2}\right)^{-\mu/2}. \quad (2)$$

Using values from ref. [60] for cratering constants (Extended Data Table 2), then

$$\frac{R}{a} = 1.306 \left(\frac{\delta}{\rho}\right)^{0.4} \left(\frac{Y}{\rho U^2}\right)^{-0.205}. \quad (3)$$

One of the key parameters that affects the derived age for strength scaling is the magnitude of the strength. Direct measurements of the cratering strength of Bennu do not exist, so assumptions must be made about the strength properties of Bennu's surface. Earlier work[23] used 0.18 MPa. Analysis[20] from the SCI experiment derives a maximum effective cratering strength on Ryugu of 1.3 Pa, although ultimately concluding that the artificial crater made by the SCI experiment formed in the gravity regime. Analysis of crater ejecta on Bennu[50] also indicates very low cratering strengths on Bennu. A strength of 10 Pa generates results very similar to gravity scaling. For strength of 1–2 Pa, the difference between strength and gravity would be even smaller.

Gravity regime. Once lithostatic stresses caused by gravitational overburden exceed the strength of a target, the formation of a crater occurs in the gravity regime, which[60] can be cast as

$$R = \left(\frac{\rho}{m_\mathrm{p}}\right)^{-1/3} H_1 \left(\frac{\rho}{\delta}\right)^{\frac{2+\mu-6\nu}{3(2+\mu)}} \left(\frac{ga}{U^2}\right)^{-\frac{\mu}{2+\mu}}. \quad (4)$$

TS2018. TS2018 conducted a series of experiments, evaluating crater morphology in granular targets as a function of impact energy and the relative sizes between the impactor and a typical target particle size. They expand traditional π-scaling relationships, such as those in equations (1)–(4) to include two additional dimensionless ratios:

$$\xi = \frac{0.5\, m_\mathrm{p} U^2}{m_\mathrm{t} Q_\mathrm{D}^*}, \quad (5)$$

which is the ratio of the impactor kinetic energy to the target boulder disruption specific energy, and

$$\psi = \frac{D_p}{D_t}, \tag{6}$$

which is the ratio of the impactor diameter to the target diameter. Granular surfaces, with particle sizes comparable to impactor sizes, have two different armouring regimes[17]. When $\xi > 1$ and $\psi < 1$ (called 'armouring regime I' in ref. [17]), that is, when the impactor kinetic energy is greater than the disruption energy of the target particle and the impactor diameter is smaller than the mean target particle diameter, an impact crater forms with a smaller diameter than would be expected using traditional scaling relationships. When both $\xi < 1$ and $\psi < 1$ (called 'armouring regime II' in ref. [17]), this corresponds to the creation of an impact crater in the target particle or in between target particles, without particle disruption. Such a crater may not be discernible in a surface comprising the ensemble of particles.

On the basis of these observations, TS2018 modified the traditional π-scaling relationships to account for these behaviours in coarse particulate targets, with

$$\pi_V^* = K_1 \left[\pi_2^* \, \pi_4^{-1/3} + K_2 \xi^{\frac{-(2+\mu_2)}{2}} \right]^{\frac{-3\mu_1}{2+\mu_1}}. \tag{7}$$

They found that crater diameters in armouring regime I fall between the strength- and gravity-regime diameters at smaller impactor diameters, and as impactor diameter grows, the resulting crater diameter converges to gravity-scaled diameters. ψ does not appear in the scaling relationships, although it plays an important role when establishing whether an impact forms a crater or disrupts a boulder without forming a crater.

To obtain a crater diameter (radius) from equation (7), we note that the simple, dimensionless ratio form of π_V^* is (TS2018, their equation (8))

$$\pi_V^* = \frac{\rho_t \, V_c}{m_t + m_p}, \tag{8}$$

which we invert to solve for V_c as

$$V_c = \frac{m_t + m_p}{\rho_t} \pi_V^*. \tag{9}$$

We assume that $V_c \propto R_c^3$, in particular, that V_c is a paraboloid of revolution, $V_c = 0.5\pi R_c^2 h$. Small craters on Bennu have varying depth-to-diameter values, though a typical Bennu value[37] for craters >10 m in diameter is 0.1. Adopting $h = 0.1$ and $D = 0.2\,R_c$, then $V_c = 0.314\,R_c^3$. Solving for R_c, and substituting into equations (9) and (5), then

$$R_c = \left[\left(\frac{m_t + m_p}{0.314\rho_t} \right) K_1 \left[\pi_2^* \, \pi_4^{-1/3} + K_2 \xi^{\frac{-(2+\mu_2)}{2}} \right]^{\frac{-3\mu_1}{2+\mu_1}} \right]^{1/3}, \tag{10}$$

which defines the transient crater radius using the scaling-relationship parameters for TS2018. The transient and final crater sizes differ for a weak target because over-steepened crater walls collapse, which causes the crater rim to retreat, thereby enlarging the final crater. We use a factor of 1.18 to convert from the transient to final crater radius[61].

Boulder properties appear in this scaling through their size, density and Q_D^*, their disruption specific energy.

We implemented the TS2018 scaling relationship by sampling SFDs for both the impactor diameter (see next section) and the target boulder diameter. The observed population of boulders on Bennu's surface can be approximated by a power law. Reference [46] reports a cumulative power-law index of -2.5 ± 0.2 for average-albedo boulders, although these data had an estimated completeness limit of ~8 m, larger than the smallest visible impact craters from data acquired later in the mission. More recent analysis[47] examined boulder populations in multiple image datasets, from global, to regional, to local, and find an overall best-fit cumulative exponent of -2.5 ± 0.1. Thus, we generated boulders according to a -2.5 cumulative power law. Because the probability of hitting a boulder is based on its area rather than its diameter, we generated boulder diameters converting the diameter-based SFD to an area-based SFD, and sampling by the cumulative fractional area covered by the boulder population. Extended Data Fig. 3a shows a simple flowchart of our implementation of TS2018 scaling for a given modelled age.

From our simulations, we determined that the shape and location of the fishhook in the crater SFD are the result of:

- The presence of three cratering regimes: (1) impact energies large enough that a crater always forms, forming larger-diameter craters, (2) a transition regime in which a crater may or may not form depending on the impact energy and target-boulder disruption energy and (3) a small-diameter regime in which no craters form in the bulk asteroid surface.
- The elimination of a one-to-one relationship between impactor size and crater size for a set of selected scaling parameters. In gravity or strength regimes for chosen parameters, a given-sized impactor will always make the same-sized crater. In contrast, our implementation means that a given-sized impactor could strike a range of boulder sizes, and the outcome of the impact depends on the relative energies of the impactor and target boulder. Thus, a single impactor will make a crater in a range of sizes, depending on the size of the target boulder. As a result, the boulder SFD is a relevant parameter: the relative proportions of small and large boulders contribute to the likelihood that an impactor will strike a given boulder size.
- The functional form of Q_D^* affects the height and diameter of the SFD peak.

Derivation of surface ages using MBA and NEA fluxes. The surface age derived from impact craters depends on the scaling relationship used to translate from impactor to crater, as well as the flux of objects striking the surface. Although Bennu is now an NEA, it originated from the main belt[48] and has experienced both MBA and NEA impact fluxes. We model the crater population from each source to constrain Bennu's surface age.

The age estimated from the crater population is the crater retention age, that is, how long that surface holds on to craters of a given size[62]. The number and sizes of craters on a surface are a function of the impact flux, the scaling law, the dynamical evolution of the object and the processes erasing the craters. If any process erases craters, the crater retention age will differ from the age of the body itself. The ages derived below are the crater retention ages of Bennu, which as we will explore further, likely differ from the age that Bennu has been an independent object orbiting the Sun.

Main belt impactors. Reference [45] provides the incremental flux of impactors in the main belt down to about 12 cm diameter. In addition, it provides a range of impact probabilities for Bennu as it evolved across the main belt. We use their average value of $_{Pi} = 3.29 \times 10^{-18}\,\mathrm{km^{-2}\,yr^{-1}}$. To combine the incremental flux with the impact probability to obtain ages, we turn the differential flux into a cumulative flux, N_{CF}. In addition, the smallest craters on Bennu are made from impactors smaller than 12 cm. To derive the population of smaller sizes, we fit a power law to N_{CF} (ref. [45]), with a coefficient of 2.891×10^{-14} and index of -2.7. Observations of bolides in Earth's atmosphere[49] show a similar index for metre-scale objects. Although the MBA and NEA populations differ in total number, they consist of similar bodies (the NEA population is derived from the MBA population), and it is reasonable to expect the SFDs at small sizes, in part driven by collisional evolution, to be similar.

The resulting number of impactors N_i for a given age T is

$$N_i(D > D') = \frac{T A_x \, P_i \, N_{CF}}{4\pi}, \tag{11}$$

where A_x is Bennu's cross-sectional area. We then apply the crater scaling relationships (see previous section) to the impactors to create a model crater population for that age.

NEA impactor flux. We bound the possible lifetime of Bennu as an NEA by examining the accumulation of a model crater population using just the expected NEA flux. To estimate the flux on Bennu as an NEA, we start with ref. [49], which analysed observations of bolides disrupting in Earth's atmosphere, and from that analysis derive the flux of small meteors in near-Earth space. They report the cumulative number of objects striking the Earth each year as

$$\log N = c_0 - a_0 \log D_p, \tag{12}$$

which is

$$N = 10^{c_0} D_p^{-a_0}. \tag{13}$$

To get the cumulative number of impacts per square kilometre per year, we normalize equation (13) by Earth's cross-sectional area to obtain

$$N = \frac{10^{c_0}}{\pi R_E^2} D_p^{-a_0}. \tag{14}$$

Reference [49] reports $c_0 = 1.568$ and $a_0 = 2.7$, and if we assume that $R_E = 6{,}378$ km, then $N = 5.46 \times 10^{-8}\, D_p^{-2.7}$ per km² per year. In addition to a change in flux, the average impact speed increases[63] to 18.4 km s⁻¹.

Finally, we apply a correction factor to remove the gravitational focusing effect of Earth from the flux we apply to Bennu. The v_{inf} of an object approaching the Earth is

$$v_{inf} = \left(v_i^2 - v_{esc}^2 \right)^{1/2}. \tag{15}$$

Reference [49] uses $v_i = 20.3\,\mathrm{km\,s^{-1}}$, and for a v_{esc} (Earth escape speed) value of 11.2 km s⁻¹, then $v_{inf} = 16.9\,\mathrm{km\,s^{-1}}$. Then, the enhancement factor due to gravitational focusing for the Earth is

$$f_g = 1 + \frac{v_{esc}^2}{v_{inf}^2} = 1.44. \quad (16)$$

To remove gravitational focusing from the flux at Bennu, we apply the inverse of this factor to equation (14):

$$N = \frac{1}{f_g}\frac{10}{\pi R_E^2} c_0 D_p^{-a_0}. \quad (17)$$

We apply both the MBA and NEA flux models to match the small-crater SFD peak and largest craters. We compare the model results and observations by using

$$\chi^2 = \frac{1}{M}\sum_{j=1}^{M}\frac{\left(N_{m,j} - N_{o,j}\right)^2}{N_{m,j}}, \quad (18)$$

where χ^2 is the normalized least-squares error between the differential crater SFD values of the model population, $N_{m,j}$, and the observed crater population, $N_{o,j}$, and M is the number of diameter bins used. To evaluate the sensitivity of the fit between the observed and modelled crater populations, we used different sets of diameter bins. Extended Data Fig. 3b,c illustrates the combinations of diameter bins we used for the small- and large-crater fits. For the small craters we used ten different bin sets, for the large craters we used five different bin sets.

Extended Data Fig. 4 plots the residuals for the NEA flux. There is a consistent minimum residual for small craters across a relatively narrow range of ages, from 1.6 to 2.2 Myr (Extended Data Fig. 4a–f). The minimum residuals for the large craters (Extended Data Fig. 4g–k) correspond to crater retention ages that significantly exceed Bennu's transition to an NEA, as well as the maximum lifetime expected for NEAs, thus we conclude that the large craters are a product of the MBA flux. Unlike the small craters, there is not a consistent minimum across the bin sets for a given age. This is due to the irregular form of the largest bins, and the increasing departure of the modelled population at progressively smaller diameters (Fig. 4b). The broad minimum is because the modelled population can 'split the difference' between the two largest bins (A and B) and the third largest bin (C) (Extended Data Fig. 3b,c).

Extended Data Fig. 5 plots the crater diameter as a function of impactor diameter for a 30 cm target boulder using the minimum and maximum surface acceleration values on Bennu. The difference is negligible for crater diameters observed on Bennu, demonstrating that using the average gravitational acceleration is sufficient for evaluating the crater retention ages using the NEA or MBA fluxes.

Extended Data Fig. 6 plots the residuals between the MBA flux and large-crater bins, as well as the model outcomes for the minimum and maximum age with minimum residuals.

Extended Data Fig. 8a plots the model crater populations for the 2.6 Myr NEA flux (corresponding to the most likely length of time that Bennu's impact flux has been entirely decoupled from the main belt[48]), the expected median lifetime of Bennu as an NEA. The TS2018 and strength-scaled model craters exceed the observations for diameters <10 m, indicating that all craters smaller than this size formed since Bennu has been dynamically decoupled from the main belt. This figure also shows that a 100 Pa cratering strength produces results consistent with TS2018 scaling.

Extended Data Fig. 8b–d plots the cumulative, differential and relative formats of the crater populations observed on Bennu, Ryugu[6] and Itokawa[7].

Data availability

OCAMS images from the Approach, Orbital A, and Detailed Survey mission phases[64], and OLA data from the Orbital B mission phase[65], are available via the Planetary Data System (https://sbn.psi.edu/pds/resource/orex/). The crater measurements (diameter, latitude and longitude of centres) will be available with this publication via FigShare.

Code availability

The SMBT[30] is available at http://sbmt.jhuapl.edu/.

References

56. Golish, D. R. et al. Ground and in-flight calibration of the OSIRIS-REx camera suite. *Space Sci. Rev.* **216**, 12 (2020).
57. DellaGiustina, D. N. et al. Overcoming the challenges associated with image-based mapping of small bodies in preparation for the OSIRIS-REx mission to (101955) Bennu. *Earth Space Sci.* **5**, 929–949 (2018).
58. Gay, P.L., Lehan, C. & the CosmoQuest Coders Den Volunteers. Citizen Science Builder. *GitHub* https://github.com/CosmoQuestX/CSB7.0 (2020).
59. Scully, J. E. C. Team, C. B. et al. in *Lunar and Planetary Science Conference* (vol. 44, p. 2860) (2013).
60. Housen, K. R. & Holsapple, K. A. Ejecta from impact craters. *Icarus* **211**, 856–875 (2011).
61. Chapman, C. R & McKinnon, W. B. in *Satellites* (eds Burns J. A. & Matthews M. S.) (Univ. of Arizona Press, 1986).
62. Hartmann, W. K. Martian cratering. *Icarus* **5**, 565–576 (1966).
63. Bottke, W. F., Nolan, M. C., Greenberg, R. & Kolvoord, R. A. Velocity distributions among colliding asteroids. *Icarus* **107**, 255–268 (1994).
64. Rizk, B., Drouet d'Aubigny, C., Golish, D., DellaGiustina D. N. & Lauretta D.S., Origins, Spectral Interpretation, Resource Identification, Security, Regolith Explorer (OSIRIS-REx): OSIRIS-REx camera suite (OCAMS) bundle, urn:nasa:pds:orex.ocams (NASA Planetary Data System, Small Bodies Node, https://arcnav.psi.edu/urn:nasa:pds:context:instrument:ocams.orex 2019).
65. Daly, M.; Barnouin, O.; Espiritu, R.; and Lauretta, D., Origins, Spectral Interpretation, Resource Identification, Security, Regolith Explorer (OSIRIS-REx): OSIRIS-REx Laser Altimeter Bundle, urn:nasa:pds:orex.ola (NASA Planetary Data System, Small Bodies Node, https://arcnav.psi.edu/urn:nasa:pds:context:instrument:ola.orex 2019).

Acknowledgements

This material is based upon work supported by NASA under contracts NNG12FD66C and NNM10AA11C issued through the New Frontiers Program. The OLA build and Canadian science support were provided by a contract with the Canadian Space Agency. We are grateful to the entire OSIRIS-REx team for making the encounter with Bennu possible. The efforts of CosmoQuest's Bennu mappers contributed to the measurement of Bennu's crater population. A complete list of their names is available at CosmoQuest.org/Bennu/credits. S.R.S. acknowledges support from NASA grant no. 80NSSC18K0226 as part of the NASA OSIRIS-REx Participating Scientist Program. P.M. acknowledges funding from the French space agency CNES, from the European Union's Horizon 2020 research and innovation program under grant agreement no. 870377 (project NEO-MAPP) and from the Academies of Excellence of the IDEX JEDI of Université Côte d'Azur. M.P. was supported for this research by the Italian Space Agency (ASI) under ASI-INAF agreement no. 2017-37-H.0.

Author contributions

E.B.B. led data collection, data analysis and writing. D.T. co-led the data collection and contributed to the analysis and writing. R.T.D. developed the DTMs used to analyse the craters and contributed to the analysis and writing. C.A.B. led the OSIRIS-REx CosmoQuest citizen-scientist measurements of impact craters on Bennu and contributed to the writing. O.S.B., K.J.W., R.-L.B., W.F.B., K.N.B., H.C.C., M.G.D. and D.N.D. contributed to data analysis and writing. E.R.J., T.J.M. and J.P.D. contributed to data collection. P.L.G. is lead of the CosmoQuest program and contributed to the writing. J.I.B., J.N., J.P. and S.Stewart provided independent evaluations of CosmoQuest measurements. S.Shwartz, P.M. and M.P. contributed to the writing. D.S.L. is principal investigator of the OSIRIS-REx mission and contributed to the writing.

Competing interests

The authors declare no competing interests.

Additional information

Extended data is available for this paper at https://doi.org/10.1038/s41561-022-00914-5.

Supplementary information The online version contains supplementary material available at https://doi.org/10.1038/s41561-022-00914-5.

Correspondence and requests for materials should be addressed to E. B. Bierhaus.

Peer review information *Nature Geoscience* thanks Ralf Jaumann, Masahiko Arakawa and Jennifer Anderson for their contribution to the peer review of this work. Primary handling editors Tamara Goldin and James Super, in collaboration with the *Nature Geoscience* team.

Reprints and permissions information is available at www.nature.com/reprints.

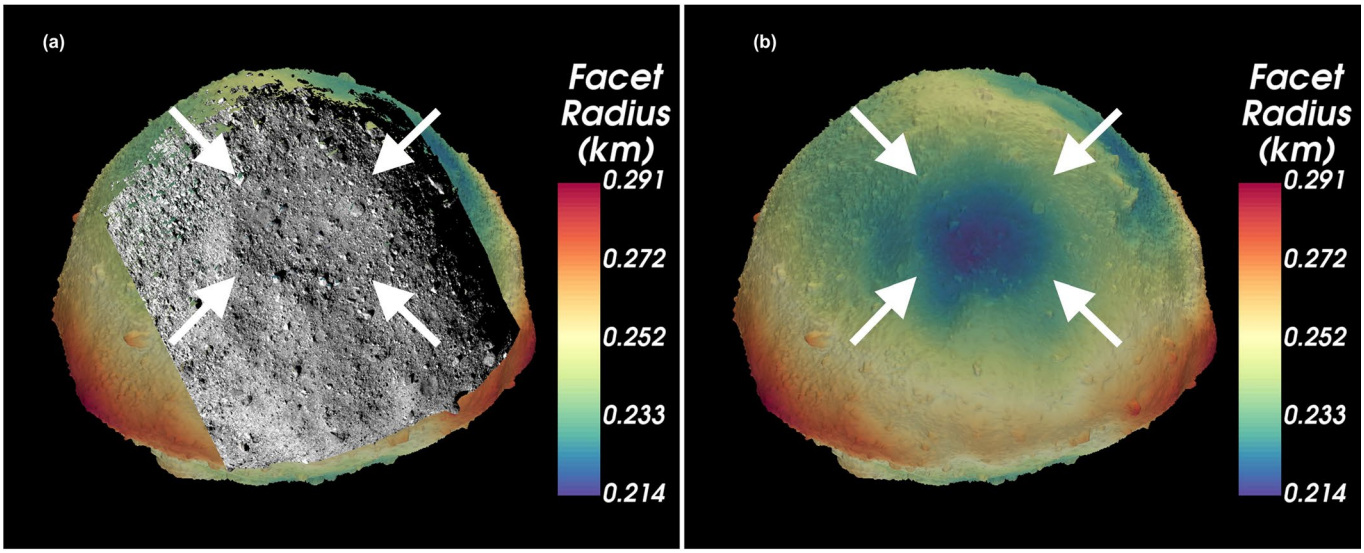

Extended Data Fig. 1 | Example identification of a large crater on Bennu. A 141-m-diameter crater on Bennu, centered at 55.7°N and 62.7°E. White arrows in both frames indicate the crater location. **a**, PolyCam image 20181202t050321s325_pol_iofl2pan projected onto the shape model. **b**, The shape model only, colorized by facet radius. The images collected during the spacecraft's final approach (acquired in early December of 2018), in conjunction with the shape model, were used to identify and measure large craters on Bennu.

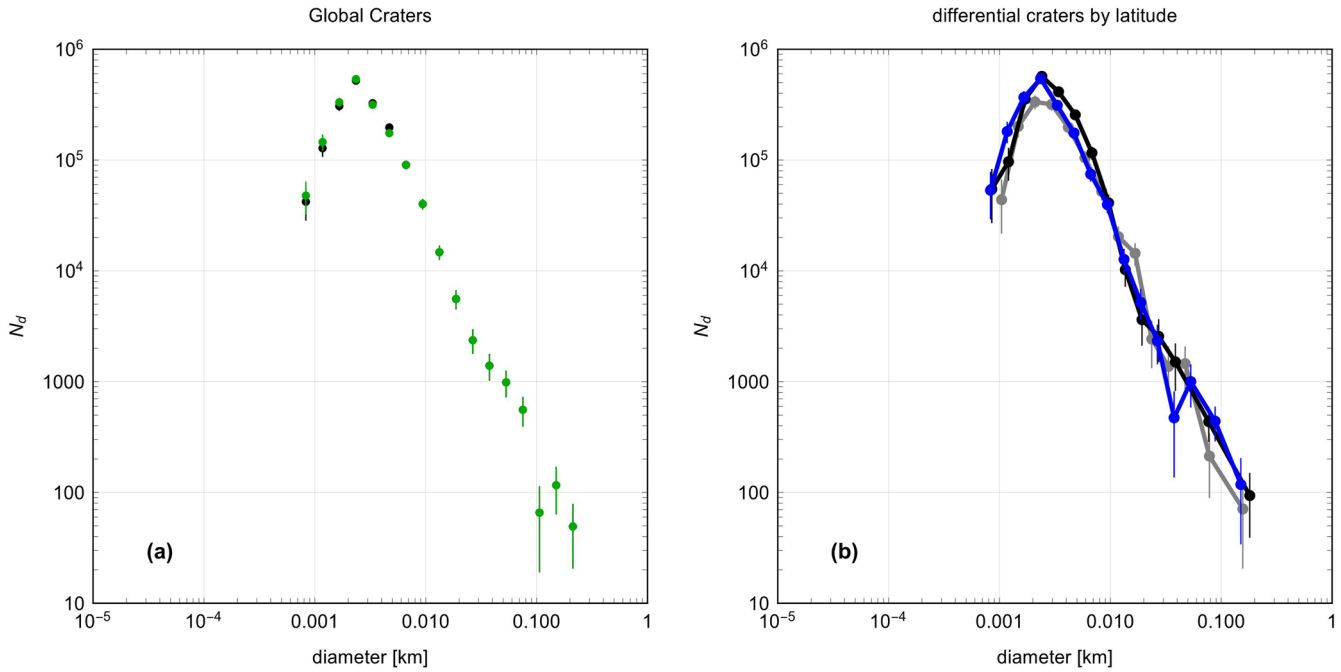

Extended Data Fig. 2 | Bennu's crater abundance as a function of latitude and slope. a, The global SFD of Bennu in differential format. The black data points are all craters, normalized by Bennu's global surface area. The green points are a population that includes all craters within ±60° latitude, and craters > 5 m diameter for higher latitudes. The difference is a small vertical shift in the differential values for craters < 5 m, the nature of the fishhook shape is unchanged. **b**, The differential crater populations for three distinct slope/latitude regions (Scheeres et al. 2019) on Bennu: the gray data are for craters < -20°S, the black data are for craters >+20°N, and the blue data are for craters within ±20° latitude. The fishhook shape is present in all three.

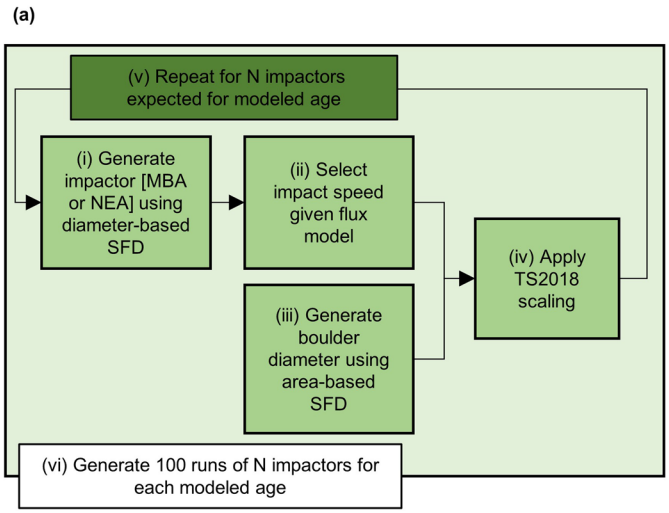

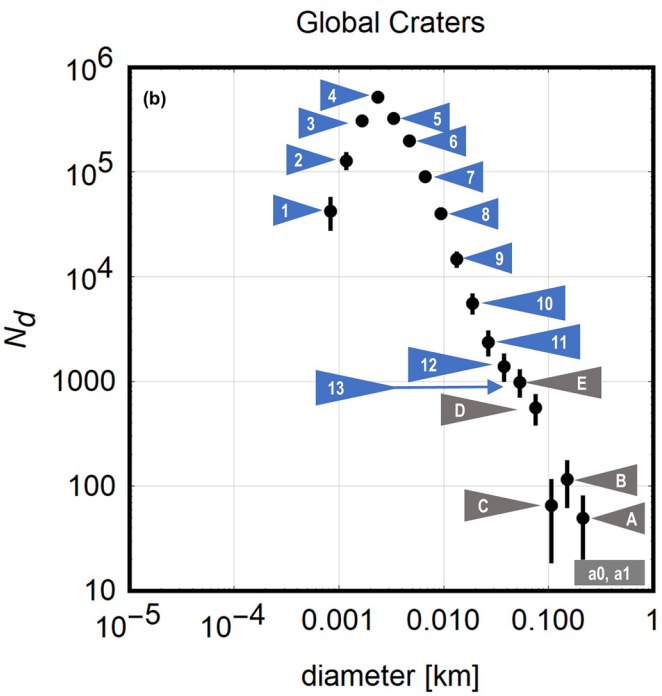

(c)

small crater bin sets		large crater bin sets	
bin set	bins used	bin set	bins used
1	4	1	a0, a1, A
2	3, 4, 5	2	a0, a1, A, B
3	2, 3, 4, 5, 6	3	a0, a1, A, B, C
4	2, 3, 4, 5, 6, 7	4	a0, a1, A, B, C, D
5	2, 3, 4, 5, 6, 7, 8	5	a0, a1, A, B, C, D, E
6	2, 3, 4, 5, 6, 7, 8, 9		
7	2, 3, 4, 5, 6, 7, 8, 9, 10		
8	2, 3, 4, 5, 6, 7, 8, 9, 10, 11		
9	2, 3, 4, 5, 6, 7, 8, 9, 10, 11, 12		
10	2, 3, 4, 5, 6, 7, 8, 9, 10, 11, 12, 13		

Extended Data Fig. 3 | A flow chart of our process for generating simulated crater populations for a given modeled age, and definition of the diameter bins used to calculate fits between the observed and modeled crater populations. a, A flow chart of our process for generating simulated crater populations for a given modeled age: (i) generate an impactor by sampling a diameter-based power-law SFD for either an MBA or NEA flux model; (ii) assign that impactor an impact speed based on the flux model; (iii) generate a boulder by sampling an area-based power-law SFD; (iv) apply TS2018 scaling for that combination of impactor and boulder; (v) repeat steps (i)–(iv) for N impactors predicted for the model age; (vi) repeat the generation of N impactors 100 times to sample the variability at a given age. **b**,**c**, Definition of the diameter bins used to calculate fits between the observed and modeled crater populations. The plot **(b)** labels small diameter bins with a number and large diameter bins with a letter. The table **(c)** lists the diameter bins used to define the bin sets used to compare observations with the model. For example, the small-crater bin set 5 uses diameter bins 2-8, and the large-crater bin set 4 uses diameter bins A-D. The labels a0 and a1 refer to the largest bin diameters that can occur in the older ages within the simulation data, which are larger than any of the observed craters on Bennu.

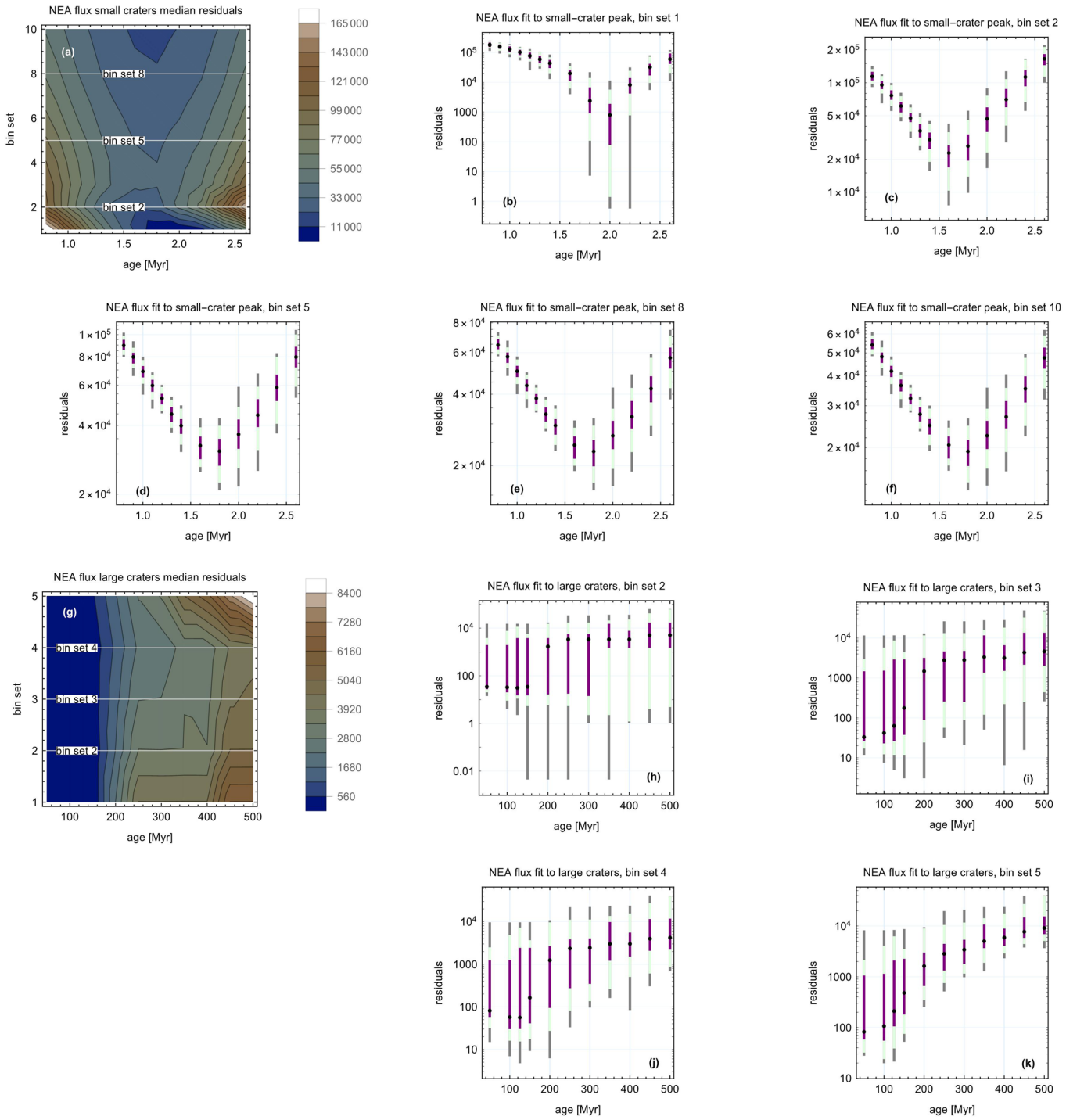

Extended Data Fig. 4 | Comparison between observed and modeled crater populations for Bennu's craters and an NEA flux. a, residuals for all combinations of bin sets and modeled ages for small craters. The residuals are in the same form as the differential SFD, which is N/(dD A), where N is the number of craters in diameter range dD, and A is the surface area used for normalization, so are in units of #/(km km2). There is a consistent minimum across all bin sets. **b**, the specific residuals for bin set 1, which consists of diameter bin 4 (Extended Data Fig. 4). The black point is the median residual for the 100 runs, the purple line spans the 25-75% range, the light-green line spans the 5-95% range, and the gray line spans the 1-99% range. **c**, **d**, **e**, and **f** are the same as **b** for bin sets 2, 5, 8, and 10, respectively. We use the 1-99% minimum residuals across the modeled ages to bound the possible ranges for the small-crater retention age. Bin set 1 establishes the maximum age at 2.2 Myr; bin set 2 establishes the minimum age at 1.6 Myr. **g**, residuals for all combinations of bin sets and NEA modeled ages for large craters. **h**, the specific residuals for bin set 2, which consists of diameter bins a0, a1, A and B (Extended Data Fig. 4). **i**, **j**, and **k** are the same as **h** for bin sets 3, 4, and 5, respectively. We use the 1-99% minimum residuals across the modeled ages to bound the possible ranges for the small-crater retention age.

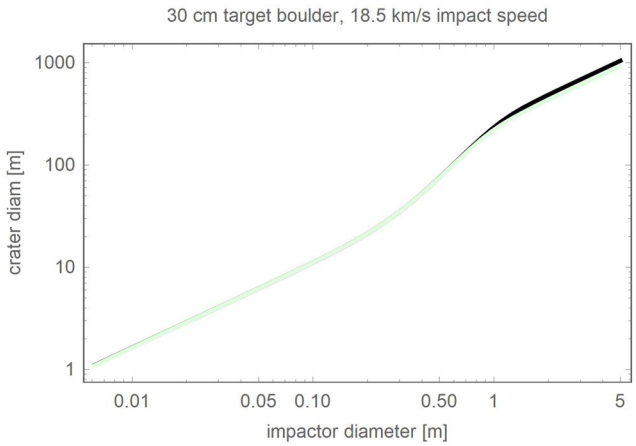

Extended Data Fig. 5 | Crater diameter as a function of impactor diameter for a 30 cm diameter target boulder and 18.5 km/s impact speed. Unlike strength and gravity scaling, which would be linear in this log-log plot, the TS2018 scaling transitions from an armoring regime at small sizes to a gravity regime at large sizes. There are two curves in the plot, one for the two gravitational end members present on Bennu (pole, light green, and equator, black), the resulting crater diameter is the same until ~200 m diameter. There's only one candidate impact feature on Bennu larger than this size, and because we calculate our ages against the binned differential data, the small difference in size for this one crater would not change its host bin. Thus, the variation in surface acceleration on Bennu does not change the outcome of our simulations.

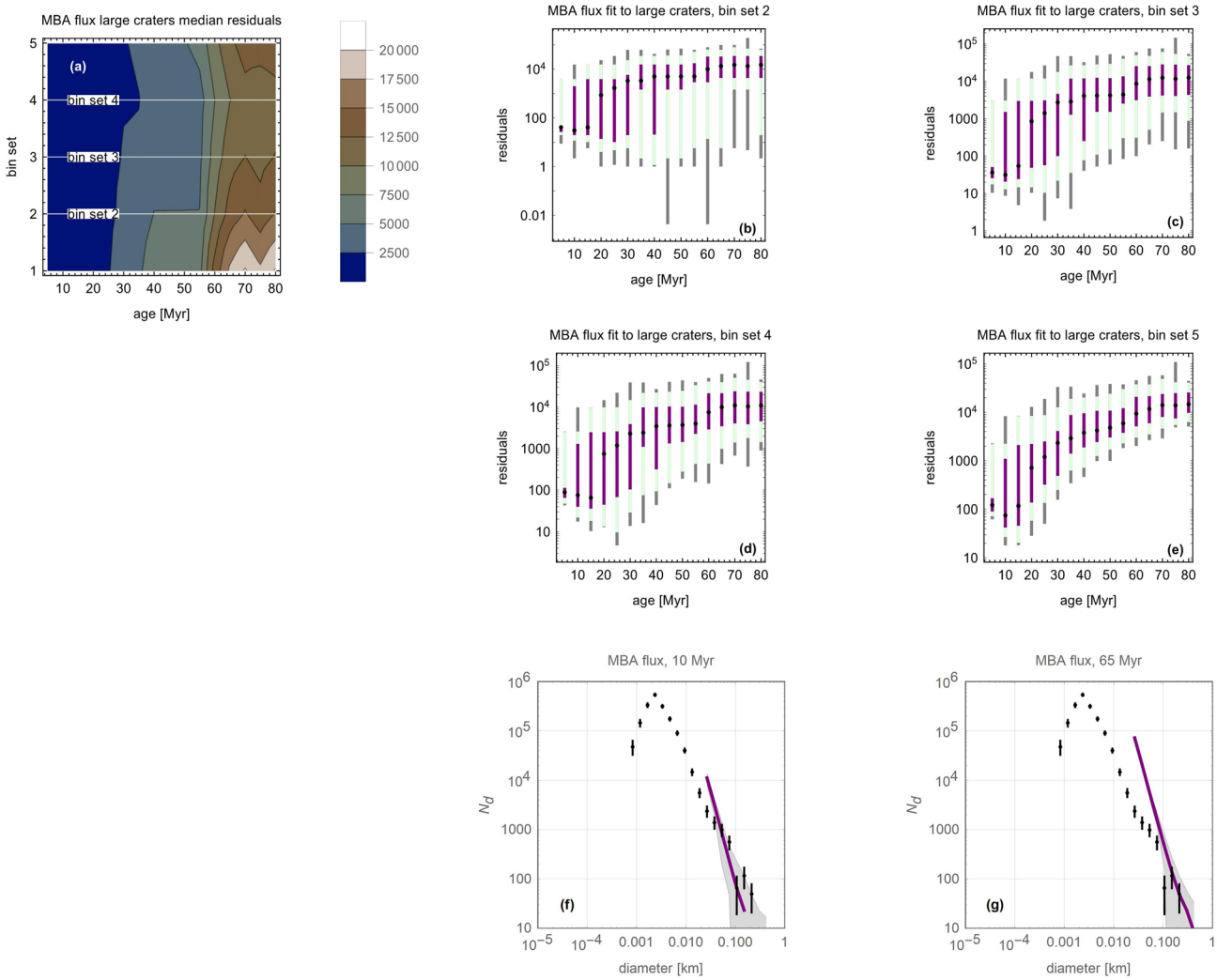

Extended Data Fig. 6 | Comparison between observed and modeled crater populations for the large craters and an MBA flux. a, residuals for all combinations of bin sets and modeled ages. The residuals are in the same form as the differential SFD, as described in Extended Data Fig. 5. **b**, the specific residuals for bin set 2, which consists of diameter bins a0, a1, A and B (Extended Data Fig. 4). Colors are as in Extended Data Fig. 5. **c**, **d**, and **e** are the same as **b** for bin sets 3, 4, and 5, respectively. We use the 1-99% minimum residuals across the modeled ages to bound the possible ranges for the small-crater retention age. The broad minimum in bin set 2 establishes the maximum age at 65 Myr; the two smallest residuals at 45 Myr and 60 Myr correspond to two cases, one for each of those ages, when there were no modeled craters larger than the observed craters, and the number of modeled craters in bin A match the observations. Bin set 5 establishes the minimum age at 10 Myr. **f** and **g** are the differential versions of the observed crater SFD and TS2018 model fits (see also Fig.1 and Fig. 4) for the 10 Myr and 65 Myr (minimum and maximum ages, respectively) with the 99% minimum residuals between observations and model results. The black data are the measured differential crater SFD of Bennu, the purple data are the median results of 100 runs, and the gray band is the 99% range of the 100 runs. Across this age span the range of the 100 modeled outcomes encompasses the variability in density seen in the three largest diameter bins.

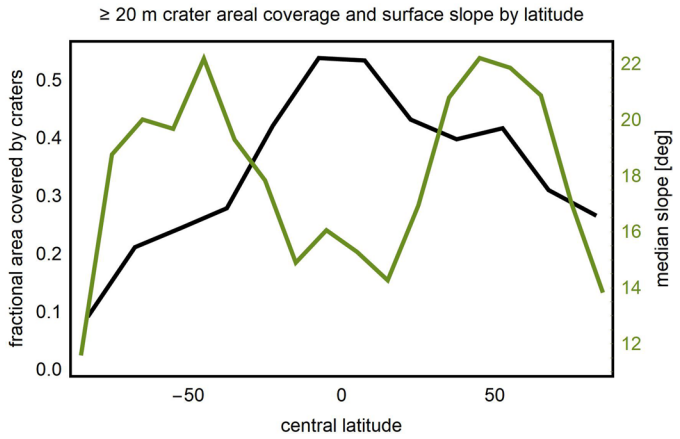

Extended Data Fig. 7 | Large craters and surface slope on Bennu. A comparison between the fractional area covered by craters ≥ 20 m diameter (black line, left-hand axis) and the median surface slope (green line, right-hand axis) as a function of latitude. Unlike the small craters, which are not correlated with slope and latitude (Extended Data Figure 2), the abundance of larger craters is correlated with latitude and slope.

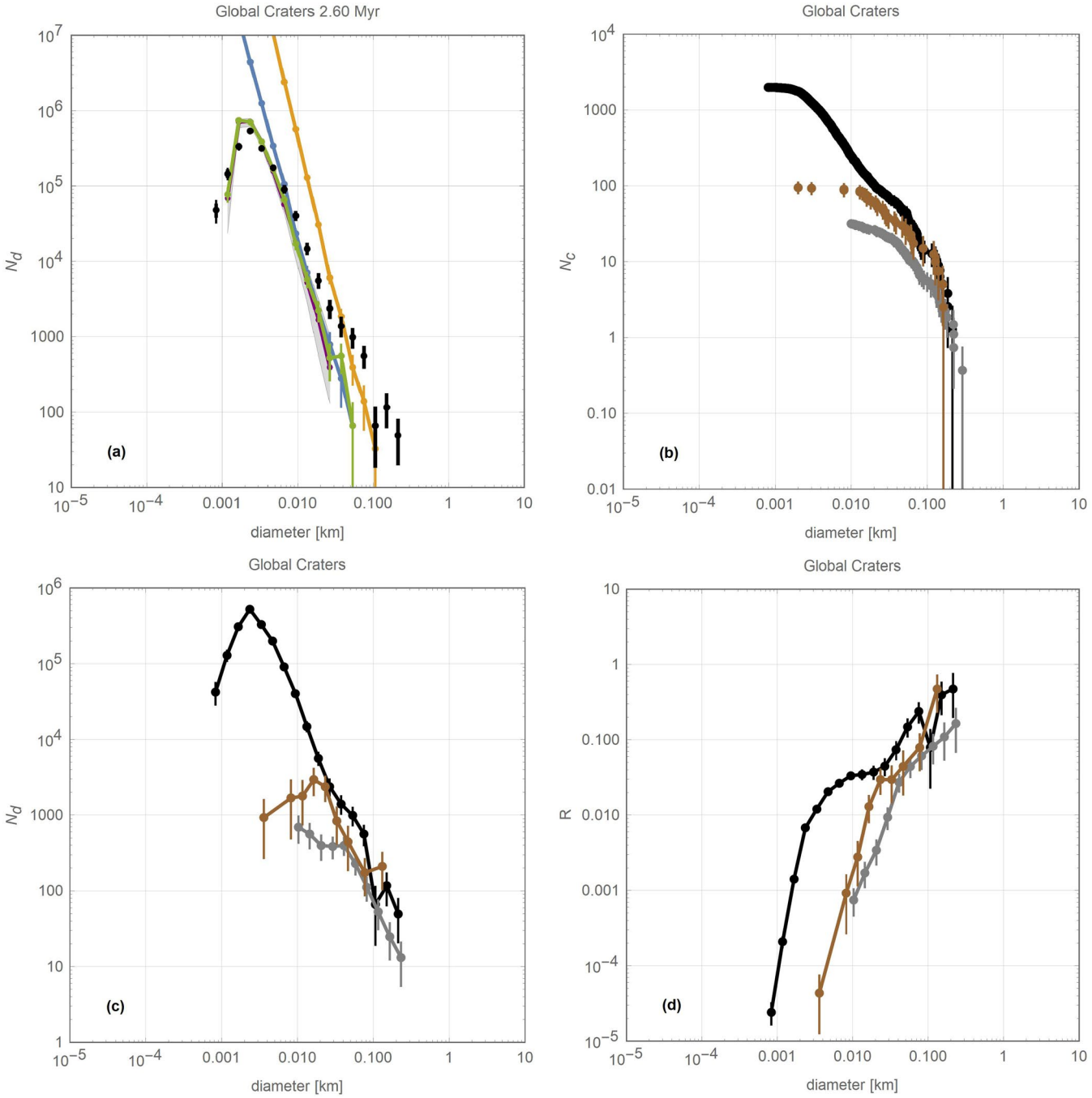

Extended Data Fig. 8 | Modeled craters for a 2.6 Myr NEA age, and comparison with Ryugu and Itokawa craters. a, This plot layers additional data sets over the style of presentation in Fig. 4. As in that figure, the black data are the measured differential crater SFD of Bennu, the purple data are the median results of 100 runs for a 2.6 Myr NEA flux model, the gray band represents the 99% range of the simulation results. Here we also include the results of one run, showing a specific case of the TS2018 scaling (green data), 100 Pa strength scaling (blue data), and gravity scaling (orange data); these data illustrate the different resulting crater populations for the three scaling laws given the same impactors. Unlike TS2018 scaling, strength- and gravity scaling continue to produce smaller craters given smaller impactors. However, above the fishhook diameter range, the strength data fall in the range of the TS2018 results, indicating that cratering strengths ≤100 Pa give comparable results to TS2018 for diameters larger than the armoring regime. TS2018 scaling approaches gravity scaling at the largest diameters on Bennu. Given that Bennu has been dynamically decoupled from the main belt for 2.6 Myr, TS2018 indicates that all craters 5 m diameter could have been formed by NEA impactors. **b**, **c**, and **d** are a comparison between Bennu's crater population (black) with Ryugu (gray) and Itokawa (brown) in cumulative, differential, and R-format, respectively.

Extended Data Table 1 | OSIRIS-REx mission data used for analysis

mission phase	dates of data used	data set	representative spatial sampling[1]	Typical phase angle	measured regions
Approach	December 1-2, 2018	PolyCam images	0.35 m/pix	~34°	Nearly global, with lower detection efficiency at high latitudes
Orbital A	January-February, 2019	MapCam images	0.11 m/pix	~95°	beyond 60 deg latitude
Detailed Survey	March 21-29, 2019	PolyCam images	0.05 m/pix	~41°	between +/- 60 deg latitude
Orbital B	June-August, 2019	OLA DTM	0.01 m	n/a	beyond 60 deg latitude
[1]spatial sampling refers to pixel scale for the images and post spacing for the lidar-derived DTMs					

Data from the mission phases used to identify, measure, and characterize Bennu's impact crater population.

Extended Data Table 2 | Symbols, units, and values used for the analysis in this paper

symbol	Value	Unit	Description
Impactor properties			
δ	2000	kg/m^3	bulk density
a	0.0025-5.0	m	radius
D_p	0.005-10.0	m	diameter
m_p	various	kg	projectile (impactor) mass
U	5.3, 18.4	km/s	mean impactor speed, MBA and NEA values[52]
θ	45	deg	assumed impact angle
Target properties			
ρ	1190	kg/m^3	Bennu bulk density
ρ_t	2000	kg/m^3	boulder density
Y	100	Pa	bulk target strength
m_t	various	kg	mass of target boulder on surface
g	5.42x10^{-5}	m/s^2	surface acceleration, a combination of surface gravity and rotation[27]
A_x	0.1886	km^2	Bennu's cross-sectional area
D_t	0.01-50.0	m	diameter of surface boulder
Housen and Holsapple crater scaling-relationships parameters			
μ	0.41	-	empirical constant, value for sand[53]
ν	0.4	-	empirical constant, multiple materials[53]
H_1	0.59	-	empirical constant, value for sand[53]
H_2	0.81	-	empirical constant, value for sand/perlite mixture[53]
D	various	m	final crater diameter (calculations done in m, plots in m or km)
R	various	m	transient crater radius
Tatsumi and Sugita (2018) crater scaling-relationship parameters			
Q^*_D	Various	J/kg	$(3.45\times10^2)\left(\frac{D_t}{2}\right)^{-0.47}+(2.72\times10^{-1})\left(\frac{D_t}{2}\right)^{0.99}$, boulder disruption specific energy[19]
Π			$\frac{m_p}{m_p+m_i}$
a*	various		$\Pi^{-1/3}a$
K_1	0.24	-	empirical constant
K_2	0.01	-	empirical constant
μ_1	0.41	-	empirical constant
μ_2	1.23	-	empirical constant
π_2^*	various	-	$\frac{a^* g}{(U*cos\theta)^2}$, the cos θ term means we apply only the vertical component of U
$\pi4$	1	-	$\frac{\rho_b}{\delta}$
V_c	various	m^3	crater volume
U*	Various	-	$\frac{(1+\epsilon)}{1+m_t/m_p}U$
ϵ	0	-	Coefficient of restitution (a 0 value is for an inelastic collision, relevant for impacts[17])
Main belt flux parameters			
P_i	3.29x10^{-18}	km^{-2} yr^{-1}	
$a_{0\,MB}$	2.7	-	exponent for the cumulative impactor power-law, extrapolated from ref.[38]
k	2.89x10^{-14}	-	coefficient for the cumulative impactor power-law, extrapolated from ref.[38]
Near-Earth flux parameters			
c_0	1.568	-	constant for the power-law SFD[44]
a_0	2.7	-	constant for the power-law SFD[44]
R_E	6378	km	Average radius of Earth

Symbols, units, and values used for the analysis in this paper.